

# Clustering in the Phase Space of Dark Matter Haloes. I. Results from the Aquarius simulations

Jesús Zavala<sup>1,2,3\*</sup> and Niayesh Afshordi<sup>1,2</sup>

<sup>1</sup>*Perimeter Institute for Theoretical Physics, 31 Caroline St. N., Waterloo, ON, N2L 2Y5, Canada*

<sup>2</sup>*Department of Physics and Astronomy, University of Waterloo, Waterloo, Ontario, N2L 3G1, Canada*

<sup>3</sup>*Canadian Institute for Theoretical Astrophysics, University of Toronto, Toronto, Ontario M5S 3H8, Canada*

2 November 2018

## ABSTRACT

We present a novel perspective on the clustering of dark matter in phase space by defining the particle phase space average density ( $P^2SAD$ ) as a two-dimensional extension of the two-point correlation function averaged within a certain volume in phase space. This statistics is a sensitive measure of small scale (sub-)structure of dark matter haloes. By analysing the structure of  $P^2SAD$  in Milky-Way-size haloes using the Aquarius simulations, we find it to be nearly universal at small scales, i.e. small separations in phase space, where substructures dominate. This remarkable universality occurs across time and in regions of substantially different ambient densities (by nearly four orders of magnitude), with typical variations in  $P^2SAD$  of a factor of a few. The maximum variations occur in regions where substructures have been strongly disrupted. The universality is also preserved across haloes of similar mass but diverse mass accretion histories and subhalo distributions. The universality is also broken at large scales, where the smooth dark matter distribution in the halo dominates. Although at small scales the structure of  $P^2SAD$  is roughly described by a subhalo model, we argue that the simulation data is better fitted by a family of superellipse contours. This functional shape is inspired by a model that extends the stable clustering hypothesis into phase space. In a companion paper, we refine this model and show its advantages as a method to obtain predictions for non-gravitational signatures of dark matter.

**Key words:** cosmology: dark matter - methods: N-body simulations.

## 1 INTRODUCTION

The gravitational clustering of dark matter has been studied intensely over the last few decades, mostly in the context of our understanding of how galaxies form and evolve within dark matter haloes. With the increase in computational power and improvement in numerical techniques,  $N$ -body simulations have given us a detailed picture of how dark matter clusters in space from large cosmological scales ( $\sim$  Gpc) down to the inner parts of galactic haloes where baryons clearly dominate the gravitational potential ( $\lesssim$  100 pc). Although such progress has led to a consensus on a variety of attributes that result from the clustering of dark matter into haloes, e.g. the universality of the density profiles (originally established in Navarro et al. 1996, 1997), there are open issues at the scales that are unresolved in

current simulations, such as the abundance, distribution and internal structure of dark matter haloes in this regime.

The clustering of dark matter at sub-kpc scales is of key importance for predictions for the hypothetical non-gravitational signatures of dark matter. Since the resolution of current simulations is many orders of magnitude above the cutoff mass of bound haloes for the majority of dark matter candidates, it is necessary to rely on uncertain extrapolations to the unresolved scales. Such uncertainty impacts the predicted experimental signals for both dark matter annihilation (indirect detection) and dark matter searches in laboratories (direct detection).

Although most studies on the distribution of dark matter have focused on spatial clustering, a more complete picture emerges by analysing its phase space structure (e.g. Bertschinger 1985; Vogelsberger et al. 2008; Diemand & Kuhlen 2008; Afshordi et al. 2009; Vogelsberger et al. 2009; Vogelsberger & White 2011; Maciejewski et al. 2011). This is particularly important

\* e-mail: jzavalaf@uwaterloo.ca

for dark matter detection efforts if the microscopic interaction of dark matter particles is velocity dependent (examples are the so-called Sommerfeld-enhanced models, e.g. Arkani-Hamed et al. 2009). In a series of two papers, we study the clustering of dark matter in the phase space of haloes using the simulation suite from the Aquarius project (Springel et al. 2008). We do so by defining a novel quantity: the particle phase space average density ( $P^2SAD$ ), which is an extension in phase space of the concept of the two-point correlation function (2PCF). In the present paper, we introduce this quantity and show, remarkably, that, at small scales (i.e. small separations in phase space), is nearly universal in time and across diversely assembled haloes, while also showing relatively small variations across spatial regions with substantially different densities.

It is important to note that  $P^2SAD$  is basically a measure of the coarse-grained phase space density (averaged around particles), as a function of coarse-graining scale. Naturally, our measurements are thus limited by the dark matter clustering resolved in the simulation. The numerically resolved coarse-graining scale is many orders of magnitude above that of the fine-grained phase space density which captures the primordial dark matter streams, and stretches and folds in phase space through the growth of structure (e.g., Vogelsberger et al. 2008). Therefore, our measurement of  $P^2SAD$  is not sensitive to these very small clustering scales. It is also different from the commonly used pseudo-phase-space density defined from halo-centric shell averages of the density  $\rho$  and velocity dispersion  $\sigma_{\text{vel}}$ :  $Q \equiv \rho/\sigma_{\text{vel}}^3$  (e.g. Taylor & Navarro 2001).

In a companion paper (Zavala & Afshordi 2013) we present a model of the  $P^2SAD$  inspired by an extension into phase space of the stable clustering hypothesis originally introduced by Davis & Peebles (1977), and recently presented in Afshordi et al. (2010) to predict the phase space clustering of gravitationally bound dark matter substructure. We refine this model by incorporating a simplified prescription of the effects of tidal disruption. Finally, we present some interesting implications for dark matter detection efforts by extrapolating this physically motivated model to the small unresolved scales.

This paper is organised as follows. In Section 2 we define  $P^2SAD$  and test the algorithm we use to compute it in a simulation. In Section 3 we investigate the behaviour of  $P^2SAD$  in the smooth halo (Section 3.1), and in substructures and across time (Section 3.2). In Section 3.3 we provide fitting functions for  $P^2SAD$  in the regime where subhaloes dominate. We study the variations of  $P^2SAD$  across regions of different ambient density and across haloes with different merger histories in Sections 3.4 and 3.5, respectively. Finally, a summary and our main conclusions are given in section 4.

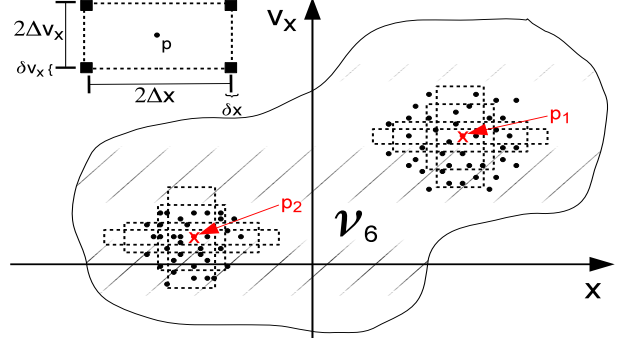


**Figure 1.** Sketch illustrating how the the particle phase space average density ( $P^2SAD$ ) is estimated in a simulation in the one-dimensional case. For each particle  $p$  in a random sample of particles in a region of volume  $\mathcal{V}_6$ , we count the number of particles  $N_p$  that lie at a separation in phase space in the corners of the rectangles of sizes  $(\Delta x - \delta x/2, \Delta v_x - \delta v_x/2)$  and  $(\Delta x + \delta x/2, \Delta v_x + \delta v_x/2)$  centred in  $p$ . The  $P^2SAD$  (Eq. 4) is then defined as the average phase space density of particles in these rectangular corners of size  $(\delta x, \delta v_x)$ . The  $P^2SAD$  is then a measure of average clustering, at the  $(\Delta x, \Delta v)$  scale, in the phase space of the region of volume  $\mathcal{V}_6$ .

## 2 PARTICLE PHASE SPACE AVERAGE DENSITY ( $P^2SAD$ )

The 2PCF between two points in phase space separated by  $\Delta \mathbf{x}$  and  $\Delta \mathbf{v}$  is given in terms of the phase space distribution:

$$\begin{aligned} & \langle f(\mathbf{x}, \mathbf{v})f(\mathbf{x} + \Delta \mathbf{x}, \mathbf{v} + \Delta \mathbf{v}) \rangle_{\mathcal{V}_6} \\ & \equiv \frac{1}{\mathcal{V}_6} \int_{\mathcal{V}_6} d^3 \mathbf{x} d^3 \mathbf{v} f(\mathbf{x}, \mathbf{v})f(\mathbf{x} + \Delta \mathbf{x}, \mathbf{v} + \Delta \mathbf{v}) \end{aligned} \quad (1)$$

where we average over a volume  $\mathcal{V}_6$  of the phase space. For convenience, we study the 2PCF in this paper by analyzing instead the mass-weighted average phase space density of dark matter, lying at spheres of radius  $\Delta x = |\Delta \mathbf{x}|$  and  $\Delta v = |\Delta \mathbf{v}|$ , in position and velocity spaces respectively:

$$\Xi(\Delta x, \Delta v) \equiv \frac{\int_{\mathcal{V}_6} d^3 \mathbf{x} d^3 \mathbf{v} f(\mathbf{x}, \mathbf{v}) \tilde{f}(\mathbf{x}, \mathbf{v}; \Delta x, \Delta v)}{\int_{\mathcal{V}_6} d^3 \mathbf{x} d^3 \mathbf{v} f(\mathbf{x}, \mathbf{v})} \quad (2)$$

where  $\tilde{f}$  is the average of  $f$  over solid angles in  $\Delta \mathbf{x}$  and  $\Delta \mathbf{v}$ :

$$\tilde{f}(\mathbf{x}, \mathbf{v}; \Delta x, \Delta v) = \frac{\int d\Omega_{\Delta \mathbf{x}} d\Omega_{\Delta \mathbf{v}} f(\mathbf{x} + \Delta \mathbf{x}, \mathbf{v} + \Delta \mathbf{v})}{\int d\Omega_{\Delta \mathbf{x}} d\Omega_{\Delta \mathbf{v}}}. \quad (3)$$

In this form,  $\Xi(\Delta x, \Delta v)$  is the auto-correlation function of the fine-grained phase space density. Since we deal with coarse-grained quantities from here on, and for reasons that become more clear in the next subsection, we call  $\Xi(\Delta x, \Delta v)$  Particle Phase Space Average Density, or in short:  $P^2SAD$ .

### 2.1 Numerical algorithm and testing

In a simulation, the dark matter is represented by a discrete set of  $N$  particles, where each has a mass  $m_p$  many orders of magnitude above the free-streaming mass of cold dark matter (CDM) particles. In this discrete representation of the dark matter density field, Eq. (2) is estimated as:

$$\Xi(\Delta x, \Delta v)_{\text{sim}} = \frac{m_p \langle N_p(\Delta x, \Delta v) \rangle_{\mathcal{V}_6}}{V_6(\Delta x, \Delta v)}, \quad (4)$$

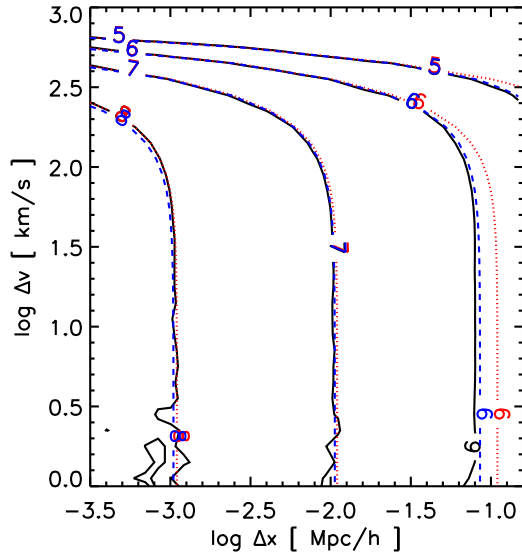


**Figure 2.** Contours of the logarithm of the particle phase space average density ( $P^2SAD$ ) for a singular isothermal sphere with a cutoff radius of  $R_c = 222.7$  kpc. The analytical result for the case  $\Delta x \ll R_c$  is shown with a dotted red line while the result of evaluating Eq. (2) numerically is shown with a dashed blue line. The result of applying the full numerical code for a Monte Carlo realization with  $6 \times 10^6$  particles is shown in black. Poisson noise starts to dominate at the lowest separations in velocity, particularly at small values of  $\Delta x$ .

where  $\langle N_p \rangle$  is the average number of simulation particles within shells of thickness  $(\delta x, \delta v)$  at a radius  $\Delta x$  and  $\Delta v$  in phase space, centred on each of the particles in the phase space volume  $\mathcal{V}_6$  (see Fig.1), and  $V_6(\Delta x, \Delta v)$  is the phase space volume of a given shell. In the limit that the mass resolution of the simulation,  $m_p \rightarrow 0$ ,  $\Xi_{\text{sim}}$  approaches  $\Xi$  in Eq. (2). This is also why we use the name Particle Phase Space Average Density, or  $P^2SAD$ , since this quantity describes the mean phase space density that a typical particle in volume  $\mathcal{V}_6$  sees at a certain separation from its position in phase space.

To compute the  $P^2SAD$  in an optimal way, we use an algorithm that selects a random sample  $N_s$  of the total particles within a given region of the simulation and computes  $\langle N_p \rangle$  within this sample. Since the relative sampling error roughly scales as  $\sim 1/\sqrt{N_s}$ , a fixed value for the sample of particles gives roughly the same “noise” level in the estimate of  $\Xi_{\text{sim}}$ , independent of the resolution of the simulation. The fraction of particles in the sample for a simulation with a total of  $N_{\text{part}}$  particles is then selected as  $f_s = \alpha \times (10^7/N_{\text{part}})$ . The sample is selected in the following way: for each of the  $N_{\text{part}}$  particles we randomly draw a number between 0 and 1 and choose the particle if this number is  $\leq f_s$ . We have found that a value of  $\alpha = 0.6$  provides negligible errors (in most of the phase space range explored in this paper) for a reasonable amount of computation time (see also Appendix). Unless otherwise stated, we use this sample size ( $N_s = 6 \times 10^6$ ) for the rest of this paper.

To test the algorithm, we generate a Monte Carlo realization of  $N_{\text{part}}$  particles following a spherically symmet-

ric distribution with a density profile corresponding to a singular isothermal sphere with a cutoff at a radius  $R_c = 222.7$  kpc ( $M = 1.37 \times 10^{12} M_\odot$ ). The corresponding phase space profile follows the Maxwell-Boltzmann distribution:

$$f(\mathbf{x}, \mathbf{v}) = \frac{A}{(2\pi\sigma_{\text{disp}}^2)^{3/2}} \exp\left[-(\phi(r) - v^2/2)/\sigma_{\text{disp}}^2\right],$$

$$\phi(r) = 2\sigma_{\text{disp}}^2 [1 + \ln(R_c/r)]; \quad r \leq R_c \quad (5)$$

where  $A = \sigma_{\text{disp}}^2/(2\pi G e^2 R_c^2)$ , with  $\sigma_{\text{disp}}$  being the velocity dispersion,  $v$  is the magnitude of the velocity vector, and we have used the fact that since the potential is central, it only depends on the radial distance  $r$ . We note that for  $r > R_c$ ,  $f = 0$  in Eq. 5.

If  $\Delta x \ll R_c$  and we assume no cutoff in the velocity distribution, then Eq. 2 can be solved analytically:

$$\Xi(\Delta x, \Delta v)_{\text{MB}} = \frac{1}{64\pi^{1/2} G \sigma_{\text{disp}} R_c \Delta x} \exp\left(\frac{-\Delta v^2}{4\sigma_{\text{disp}}^2}\right) \quad (6)$$

Recall that  $\Delta x$  and  $\Delta v$  are the radii in position and velocity space, respectively.

In Fig. 2, we show a comparison between the  $P^2SAD$  computed from the Monte Carlo realization using our algorithm (black) and from Eq. (6) (dotted red). With the exception of the region where the analytical result breaks down (i.e.  $\Delta x \sim R$ ), the agreement is very good. The correct result is recovered when Eq. (2) is solved numerically (dashed blue) for any value of  $(\Delta x, \Delta v)$ . We note that for the thickness of the shells in phase space we have used logarithmic bins equally spaced with  $\delta_{\log x} \sim 0.1$  and  $\delta_{\log v} \sim 0.1$  throughout this paper (we have checked that our results are not changed appreciably by decreasing these values).

### 3 $\Lambda$ CDM HALOES

To compute the  $P^2SAD$  in galactic  $\Lambda$ CDM haloes, we use the set of Aquarius haloes (Springel et al. 2008), which were simulated in the context of a WMAP1 cosmology and are examples of the type of Milky-Way-size haloes predicted by CDM. The Aquarius simulations are “zoom simulations” from a larger box parent simulation where a small region containing the volume of interest at  $z = 0$ , i.e., the MW-size halo up to a few times its virial radius, is re-sampled and re-simulated with a higher number of lower mass particles. The remaining volume is sampled with decreasing mass resolution, but large enough to accurately represent the long-range tidal field. In this paper we consider only the particles within the high resolution region and mainly focus on those belonging to the virialized region of the main halo (defined as gravitationally self-bound objects by the structure finder SUBFIND, Springel et al. 2001). We note that the main halo is defined through a Friends-of-Friends method and thus it has a triaxial shape.  $P^2SAD$  is clearly a function of location within the halo since its value depends on the phase space volume where the average is done,  $\mathcal{V}_6$  (see Eqs. 2-4). While most of our results refer to  $P^2SAD$  averaged over the whole virialized region of the main halo, we discuss the environmental dependence of  $P^2SAD$  in Section 3.4.

In Table 1, we list the main parameters of the set of Aquarius haloes we analyse in this paper. We focus mainly on the Aquarius-A halo that was simulated in 5 levels of

Name	$m_p[M_\odot]$	$\epsilon[\text{pc}]$	$M_{200}[M_\odot]$	$r_{200}[\text{kpc}]$
Aq-A-2	$1.370 \times 10^4$	65.8	$1.842 \times 10^{12}$	245.88
Aq-A-3	$4.911 \times 10^4$	120.5	$1.836 \times 10^{12}$	245.64
Aq-A-4	$3.929 \times 10^5$	342.5	$1.838 \times 10^{12}$	245.70
Aq-A-5	$3.143 \times 10^6$	684.9	$1.853 \times 10^{12}$	246.37
Aq-B-4	$2.242 \times 10^5$	342.5	$8.345 \times 10^{11}$	188.85
Aq-C-4	$3.213 \times 10^5$	342.5	$1.793 \times 10^{12}$	243.68
Aq-D-4	$2.677 \times 10^5$	342.5	$1.791 \times 10^{12}$	243.60
Aq-E-4	$2.604 \times 10^5$	342.5	$1.208 \times 10^{12}$	213.63

**Table 1.** Parameters of the Aquarius haloes used in this paper:  $m_p$  is the particle mass,  $\epsilon$  is the Plummer equivalent gravitational softening length,  $r_{200}$  and  $M_{200}$  are, respectively, the virial radius and mass of the halo (defined as the mass enclosed in a sphere with mean density 200 times the critical value).

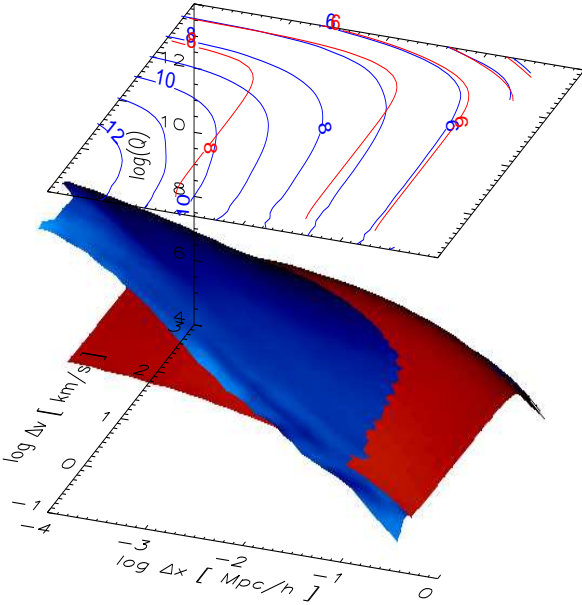


**Figure 3.** Surface and contour plot of the logarithm of the particle phase space average density ( $P^2SAD$ ) for the Aquarius A-halo resolution level 2 at  $z = 0$ . The average is done over the entire halo, including its substructure (blue) and for the smooth component of the host only (red). While the former is estimated directly from the simulation data using Eq. (4), the latter is computed analytically using an Einasto density profile with a Maxwellian velocity distribution in Eq. (2).

increasing mass and spatial resolution. In particular most of our results refer to Aq-A-2 and use the lower resolution levels for convergence tests<sup>1</sup>. The different level-4 haloes are used to analyse diverse mass aggregation histories.

<sup>1</sup> We note that we did not use the highest resolution level, Aq-A-1, since it was deemed as computationally too expensive for the computation of  $P^2SAD$ .

### 3.1 Smooth main halo component

Fig. 3 shows a surface plot of  $\log(P^2SAD)$  computed with our algorithm for the Aq-A-2 halo considering particles within the main halo and its subhaloes (blue). A 2D projection showing contours for  $\log(P^2SAD)$  is also shown on top. At large separations in  $(\Delta x, \Delta v)$ ,  $P^2SAD$  is dominated by the smooth dark matter distribution of the main halo shown in red in Fig. 3. To compute the latter, we used an Einasto density profile:

$$\rho(r) = \rho_{-2} \exp\left(\frac{-2}{\alpha_e} \left[\left(\frac{r}{r_{-2}}\right)^{\alpha_e} - 1\right]\right) \quad (7)$$

where  $\rho_{-2}$  and  $r_{-2}$  are the density and radius at the point where the logarithmic density slope is -2, and  $\alpha_e$  is the Einasto shape parameter. We used the values of these parameters from the fit to the Aq-A-2 halo given in Navarro et al. (2010):  $\alpha_e = 0.163$ ,  $\rho_{-2} = 3.9 \times 10^{15} M_\odot/\text{Mpc}^3$ ,  $r_{-2} = 15.27$  kpc. Furthermore, we assume that the velocity distribution of the smooth component is Maxwellian with no cutoff in velocity and with a radially dependent 1D velocity dispersion as given by the spherically averaged pseudo-phase space density  $\rho/\sigma_{\text{disp}}^3 \propto r^{-\chi}$  with  $\chi = -1.917$  (see Table 2 of Navarro et al. 2010, and discussion therein). The normalization of  $\sigma_{\text{disp}}$  is given by its peak value:  $\sigma_{\text{max}} \sim V_{\text{max}}/\sqrt{3}$ , where  $V_{\text{max}} = 208.49$  km/s is the maximum rotational velocity of the halo. Having assumed the density profile and the velocity distribution, we compute  $P^2SAD$  by numerically integrating Eq. (2).

There is a good match between the smooth halo modelling described before and the simulation results at large  $(\Delta x, \Delta v)$ . At close separations though, it is clear that the contribution of the smooth component is subdominant to that of substructures (see below). The main features of the structure of  $\Xi(\Delta x, \Delta v)$  coming from the smooth dark matter distribution can actually be explained by using the analytical result found for the isothermal sphere (Eq. 6):

- Small separations in phase space in Fig. 3 are denser in phase space due to the scaling of  $\Xi$  with  $\Delta x$  and  $\Delta v$ ; the former is related to the density profile making  $\Xi \propto 1/\Delta x$  for the isothermal sphere, while for CDM haloes the scaling varies due to the radial change of the logarithmic density slope.
- Since  $\Xi(\Delta x = \text{cte}, \Delta v \ll \sigma_{\text{disp}}) \sim \text{cte}$ , the contours of constant phase space density are vertical at small  $\Delta v$ . Once the velocity gets closer to the velocity dispersion  $\sigma_{\text{disp}}$ , the number of particles starts to decrease rapidly. For the isothermal sphere, the value of  $\sigma_{\text{disp}}$  is independent of radius and this is why the contours of constant  $P^2SAD$  bend at the same value of  $\Delta v$ . For the CDM case however, the velocity dispersion is a function of radius, which explains why the “bend” occurs at smaller values of  $\Delta v$  for smaller values of  $\Delta x$ , where the  $P^2SAD$  is dominated by the colder and dense central regions of the the halo centre.

### 3.2 Redshift evolution and role of substructures

Fig. 4 shows the redshift evolution of  $\log(P^2SAD)$  for the Aq-A-2 halo, from  $z = 0$  (solid black) to  $z = 3.5$  (dashed-dotted orange). To construct this figure we computed  $P^2SAD$  with our code for a sample of particles within



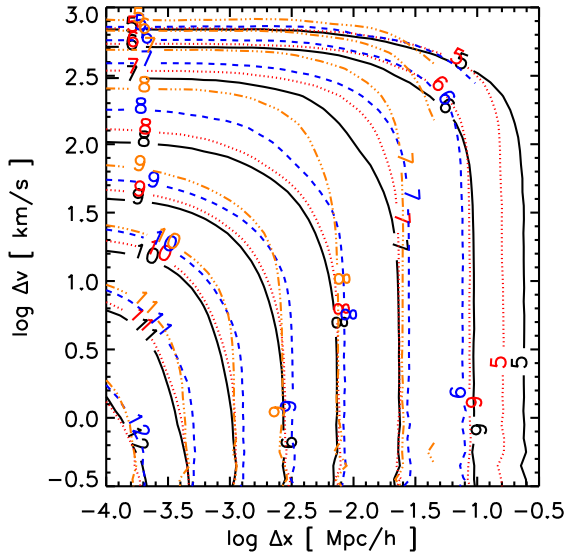


**Figure 4.** Contours of the logarithm of the particle phase space average density ( $P^2SAD$ ) for the Aq-A-2 halo at different redshifts:  $z = 0$  (solid black),  $z = 0.96$  (dotted red),  $z = 2.2$  (dashed blue) and  $z = 3.5$  (dashed-dotted orange). At each redshift, a sample from all particles within the main halo and its substructures is considered for the average.

the virialized region of the halo, identified at the given redshift. The largest evolution with redshift occurs at intermediate to large separations in velocity while there is almost no evolution at small  $\Delta v$ . In order to have a better understanding of Fig. 4, we can model the Aq-A-2 halo as a superposition of a smooth main halo and a hierarchy of subhaloes down to the minimum reliable subhalo mass in the simulation:  $\sim 10^6 M_\odot$ . At resolution level 2, a subhalo of this mass has  $\gtrsim 70$  particles, which is roughly the minimum number that we can trust in terms of global subhalo properties (see Figs. 26 and 27 of Springel et al. 2008).

We already described the properties of the main halo in Section 3.1. For the subhaloes, we assume that they have scaling properties entirely defined by their mass  $M_{\text{sub}}$  (Springel et al. 2008):  $V_{\text{max}} = 10 \text{ km s}^{-1} (M_{\text{sub}}/3.37 \times 10^7 M_\odot)^{0.29}$ ,  $\delta_V/2 = (V_{\text{max}}/H_0 r_{\text{max}})^2 = 2.9 \times 10^4 (M/10^8 M_\odot)^{-0.18}$ , where  $\delta_V$  is a measure of concentration and  $r_{\text{max}}$  is the radius where the circular velocity peaks;  $H_0$  is the value of the Hubble constant today in the  $\Lambda$ CDM cosmology. We further assume that subhaloes also have Einasto density profiles with a shape parameter that is mass-dependent (see Fig. 1 of Vera-Ciro et al. 2013). Although the scatter in this relation is large, we approximate:  $\alpha_e(M_{\text{sub}}) = 0.8, 0.65, 0.5, 0.35$  for  $M_{\text{sub}} = 10^6, 10^7, 10^8, 10^9 M_\odot$ , respectively (and interpolating for masses in between). The other two parameters of the Einasto profile are then given by  $r_{-2} = r_{\text{max}}/a(\alpha_e)$  and  $\rho_{-2} = (V_{\text{max}}/r_{-2})^2/(b(\alpha_e)G)$ , where  $a(\alpha_e)$  and  $b(\alpha_e)$  are functions of the shape parameter that are computed numerically by maximizing the circular veloc-

ity profile calculated from the enclosed mass:

$$M(r) = \frac{4\pi r_{-2}^3 \rho_{-2}}{\alpha_e} \exp\left(\frac{3\ln\alpha_e + 2 - \ln(8)}{\alpha_e}\right) \times \gamma\left(\frac{3}{\alpha_e}, \frac{2}{\alpha_e} \left(\frac{r}{r_{-2}}\right)^{\alpha_e}\right) \quad (8)$$

where  $\gamma(c, x)$  is the lower incomplete gamma function. For example, for  $M_{\text{sub}} = 10^6 M_\odot$  ( $\alpha_e = 0.8$ ),  $a = 1.756$  and  $b = 9.35$ . Each subhalo has a cutoff radius  $r_{\text{cut}}$  which, by consistency, is given by the radius where the enclosed mass is equal to  $M_{\text{sub}}$ . The velocity distribution in subhaloes is treated in the same way as in the main host with the proper scaling given by  $\sigma_{\text{max}}(M_{\text{sub}})$  (see Sec. 3.1, below Eq. 7).

Finally, we assume that  $P^2SAD$  is mainly given by correlations among particle pairs within the main halo and within subhaloes, i.e., we only consider the 1-(sub)halo term as is typically known in the halo model. The 1-subhalo term in a given mass range is weighted by the subhalo mass fraction relative to the host, which we obtain using the following fit to the subhalo mass function (Boylan-Kolchin et al. 2010; Gao et al. 2011):

$$\frac{dN}{d\ln\mu} = \left(\frac{\mu}{\tilde{\mu}_1(z)}\right)^{a^*} \exp\left[\left(\frac{-\mu}{\mu_{\text{cut}}(z)}\right)^{b^*}\right] \left(b^* \left(\frac{-\mu}{\mu_{\text{cut}}(z)}\right)^{b^*} - a^*\right) \quad (9)$$

where  $\mu = M_{\text{sub}}/M_{200}$ , and  $a^* = -0.94$  and  $b^* = 1.2$  fit the simulation data very well (both the Aquarius haloes, and those from a larger box simulation, the Millennium II, Boylan-Kolchin et al. 2009) at all redshifts for a large range of host halo masses with slowly varying values of  $\tilde{\mu}_1(z)$  and  $\mu_{\text{cut}}(z)$  with redshift (see Eq. 3 of Gao et al. 2011).

The particle phase space average density from the main host and its subhaloes is then given by:

$$\Xi(\Delta x, \Delta v) = \Xi_{\text{host}}(\Delta x, \Delta v; M_{\text{host}}) + \int_{M_{\text{min}}}^{M_{\text{max}}} dM_{\text{sub}} \frac{dN}{dM_{\text{sub}}} \left(\frac{M_{\text{sub}}}{M_{200}}\right) \Xi_{\text{sub}}(\Delta x, \Delta v; M_{\text{sub}}) \quad (10)$$

where  $M_{\text{min}}$  is the minimum subhalo mass that is resolved in Aq-A2 ( $\sim 10^6 M_\odot$ ) and  $M_{\text{max}}$  is the largest subhalo in the simulation<sup>2</sup>. We compute  $\Xi_{\text{host}}$  and  $\Xi_{\text{sub}}$  by solving numerically Eq. (2) (due to the symmetries, the integral is 4D at the end: one radial and one angular in both, space and velocity; the latter are fully analytical if we assume no cutoff to the velocity distribution). Fig. 5 shows the comparison between the subhalo model described in this Section (dashed) and the simulation results (solid) at  $z = 0$  (black) and  $z = 3.5$  (orange). To model the smooth component of the latter, we assume that the main halo at this time is well represented by the same density profile as in  $z = 0$  but with  $r_{200}(z = 3.5) \simeq 40 \text{ kpc}$  (with an enclosed mass  $\sim 0.25 M_{200}(z = 0)$ ), i.e., we assume that the central region of the halo at  $z = 0$  was already in place at  $z = 3.5$ , and the outer boundary is simply set by  $\rho_{\text{crit}}(z)$ .

The model gives a good description of the simulated data at large and intermediate separations, with the difference mainly caused by the use of a Maxwellian velocity

<sup>2</sup> We take  $M_{\text{max}} = 5 \times 10^9 M_\odot$ . There are a few subhaloes above this mass, but they make a minimal contribution.

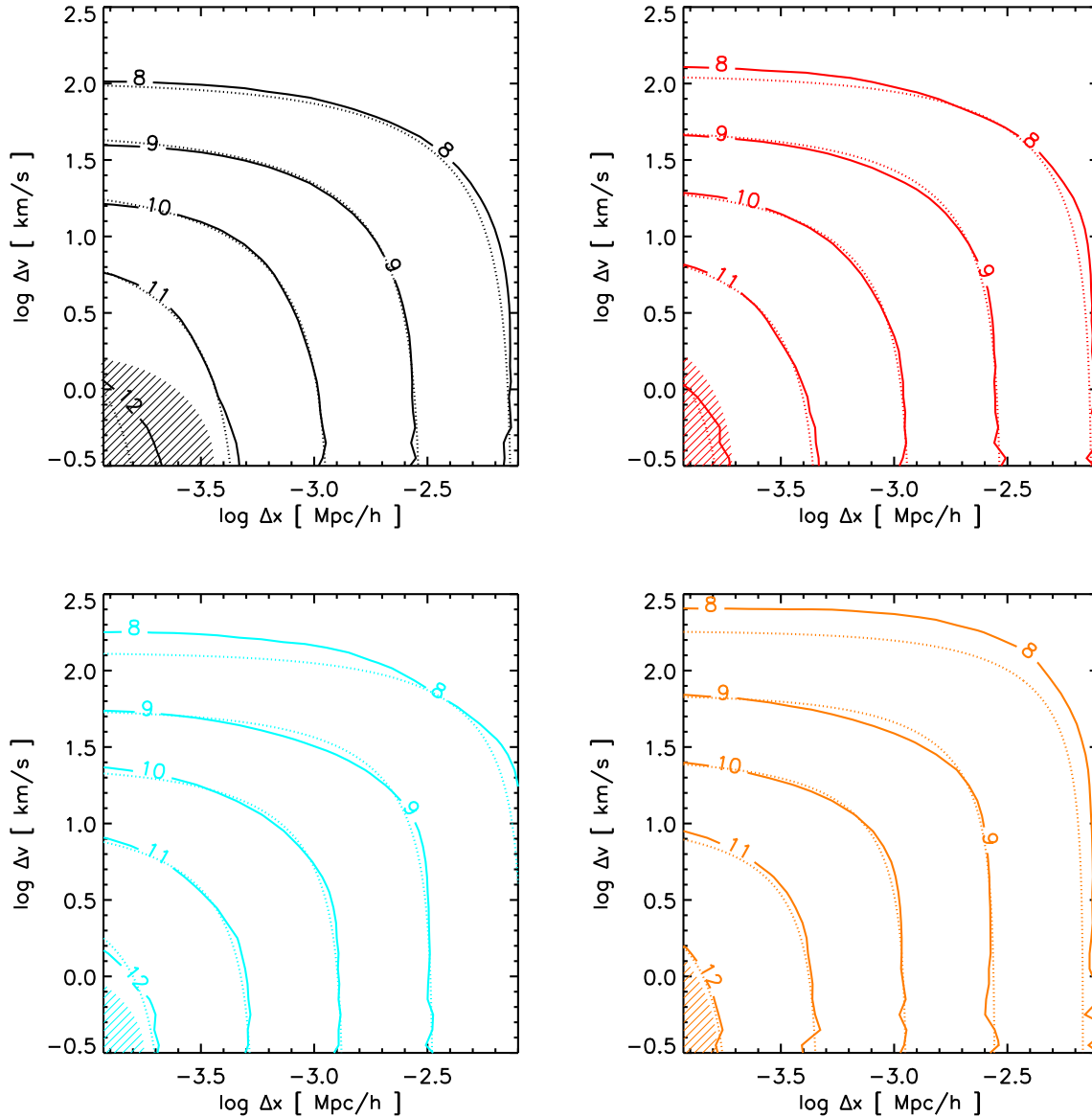


**Figure 6.** Contours of the logarithm of the particle phase space average density ( $P^2SAD$ ) of the Aq-A-2 halo (solid) and for the fitting function defined in Eqs. 11-12 (dashed) with the parameters given in Table 2. The different panels show different redshifts, clockwise from top left:  $z = 0$  (black),  $z = 0.95$  (red),  $z = 2.2$  (cyan) and  $z = 3.5$  (orange).

distribution instead of a self-consistent one corresponding to the Einasto profile. The agreement at small separations is poorer, likely due to a combined effect of the missing ingredients in the subhalo model, such as sub-substructures and a radial dependent concentration-mass relation. Nevertheless, the model is accurate to within a factor of  $< 2-3$  in most of the phase space region where convergence is good (outside the shaded areas in Fig. 5; see Appendix A).

Notice that most of the evolution of  $P^2SAD$  with redshift occurs at large separations in velocity where the smooth halo component is dominant. This dominance happens roughly at  $\Delta v \sim 100$  km/s (see Fig. 3). The model we have described in this section roughly accounts for this evolution at small  $\Delta x$ : the dense centre of the halo is already in place at  $z = 3.5$  and further accretion of material

only dilutes the coarse-grained average phase space density at lower redshifts since this new material is hotter than the cold central regions. Thus, the “inside-out” growth of the smooth component essentially accounts for most of the redshift evolution seen in Fig. 4, and is also related to the fact that the contours of constant phase space density expand in velocity but not in space at higher redshift.

### 3.3 Fitting functions for $P^2SAD$ on small scales

The model described in the previous section provides a good description of  $P^2SAD$  on large scales, but it is less accurate on small scales, where subhaloes dominate. We have found that, in this regime, a more precise description of the shape of  $P^2SAD$  is given by superellipses (Lamé curves).

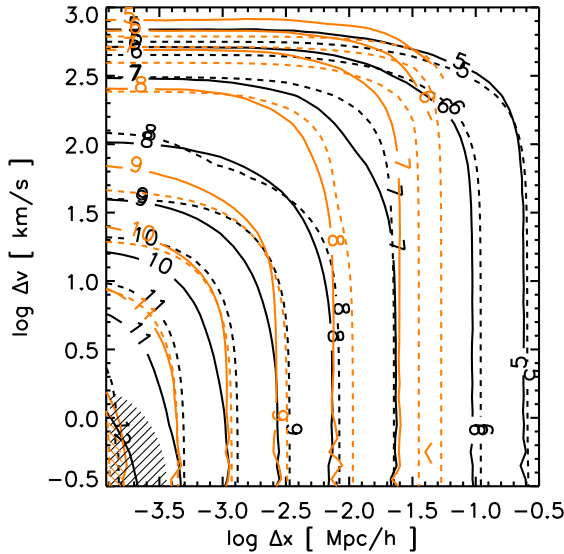


**Figure 5.** Contours of the logarithm of the particle phase space average density ( $P^2SAD$ ) for the Aq-A-2 halo (solid) and for the halo model described in the text (dashed) at two different redshifts:  $z = 0$  (black) and  $z = 3.5$  (orange). The shaded areas near the left corner encompass the region where the relative convergence between levels 3 and 2 is worse than  $\sim 1.5$  (see Appendix A).

Redshift	$q_X$ (Mpc/h)	$\alpha_X$	$q_V$ (km/s)	$\alpha_V$
0.0	11.82	-0.4	$4.5 \times 10^4$	-0.33
0.95	11.82	-0.4	$7.2 \times 10^4$	-0.35
2.2	12.0	-0.395	$1.2 \times 10^5$	-0.37
3.5	9.0	-0.415	$3.8 \times 10^5$	-0.415

**Table 2.** Values of the fitting parameters in Eq. 12. Together with Eq. 11, these parameters provide a good description of the  $P^2SAD$  at small  $(\Delta x, \Delta v)$  (see Fig. 6).

This functional shape is motivated by the stable clustering hypothesis and is the subject of an extended study in paper II of this series (Zavala & Afshordi 2013):

$$\left( \frac{\Delta x}{\mathcal{X}(\Xi)} \right)^\beta + \left( \frac{\Delta v}{\mathcal{V}(\Xi)} \right)^\beta = 1, \quad (11)$$

where  $\mathcal{X}(\Xi)$  and  $\mathcal{V}(\Xi)$  are the generalised axes of the superellipse. A reasonable fit to the simulated data at all redshifts (Fig. 6) is accomplished by the following parametrisation of the fitting parameters:

$$\begin{aligned} \beta &= \beta_0 + \beta_1(1+z) \\ \mathcal{X}(\Xi) &= q_X(z)\Xi^{\alpha_X(z)} \\ \mathcal{V}(\Xi) &= q_V(z)\Xi^{\alpha_V(z)} \end{aligned} \quad (12)$$

where  $\beta_0 = 0.67$  and  $\beta_1 = 0.08$ , while the values of the rest of the parameters are given in Table 2. Notice that with the exception of  $q_V$  all parameters change by  $\lesssim 33\%$  up to  $z = 3.5$ . We should emphasize that the fitting function

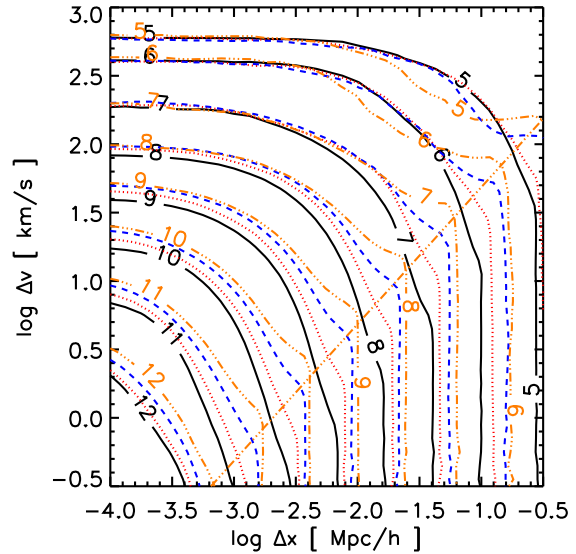


**Figure 7.** Contours of the logarithm of the particle phase space average density ( $P^2SAD$ ) for the Aq-A-2 halo at different redshifts:  $z = 0$  (black),  $z = 0.96$  (red),  $z = 2.2$  (blue) and  $z = 3.5$  (orange). The Lagrangian region containing all the high-resolution particles at  $z = 0$  is considered for all redshifts. This region covers a larger volume (highly asymmetric) than previous plots: the largest sphere within this volume has a radius of  $\sim 3.3(0.7)$  Mpc at  $z = 0(3.5)$  in physical coordinates from the center of the main halo. The mean density within this sphere is of  $\mathcal{O}(\rho_{\text{crit}})$ . The straight orange line correspond to the Hubble flow at  $z = 3.5$ , which is clearly responsible from the “bump” feature appearing more prominently at higher redshifts.

(Eq. 11) is primarily intended to describe  $P^2SAD$  in the small separation regime, which is dominated by the halo substructure, as opposed to the large separation regime, which is dominated by the smooth halo component (see Fig. 3).

### 3.4 Environmental dependence

So far, we have only analysed the particle phase space average density ( $P^2SAD$ ) averaged within a specific volume: the one defined by the virial radius of the halo. By changing the volume where this average is made, we expect to observe changes in the structure of  $P^2SAD$ . First, we show in Fig. 7 the redshift evolution of  $P^2SAD$  averaged over a larger volume, that of the Lagrangian region encompassed by all high-resolution particles at  $z = 0$ . This region is non-spherical, but the volume it covers is mostly contained within a sphere of roughly  $3.3(0.7)$  Mpc at  $z = 0$  ( $z = 3.5$ ) in physical coordinates from the centre of the main halo. This is well beyond the virial radius, and thus, the average of  $P^2SAD$  is a combination of the contribution of the main halo (including its substructures) and a plethora of low mass field haloes (with their own substructure) and unclustered matter in the surroundings of the main host. Notice that, albeit the evolution of  $P^2SAD$  in this case is stronger than in the virialized region (Fig.4), there is still only little evolution of  $P^2SAD$  at small separations.

The difference between the different volumes taken for the average can be clearly appreciated in Fig. 8 where we

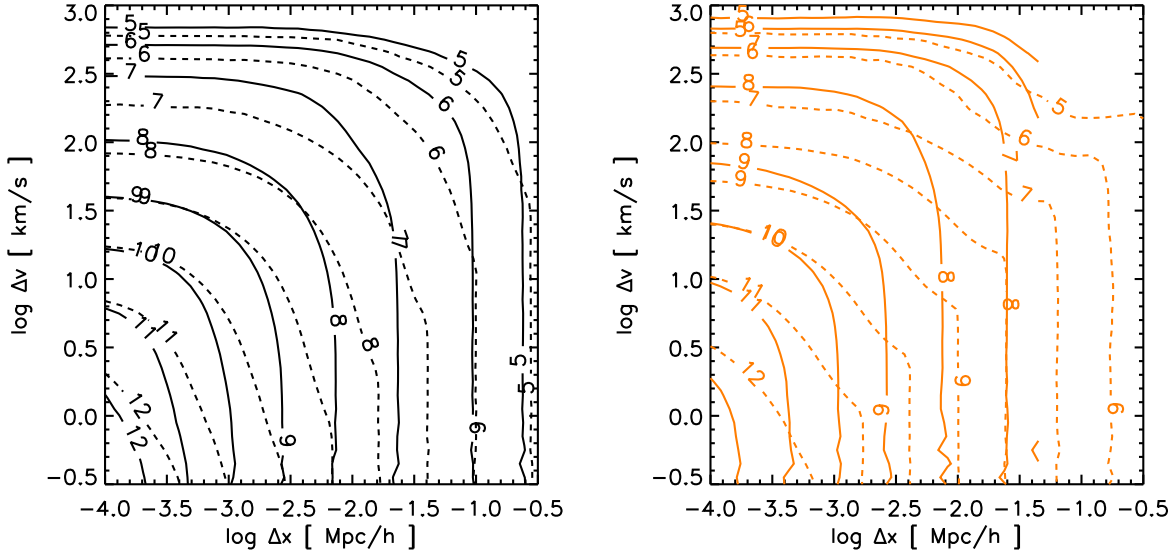


**Figure 8.** Contours of the logarithm of the particle phase space average density ( $P^2SAD$ ) for the Aq-A-2 halo averaged over different volumes: only particles within the main halo and its subhaloes (solid line), and over a larger volume defined by all the high resolution particles (see caption of Fig. 7 and text for details). The left panel is for  $z = 0$  and the right panel for  $z = 3.5$ .

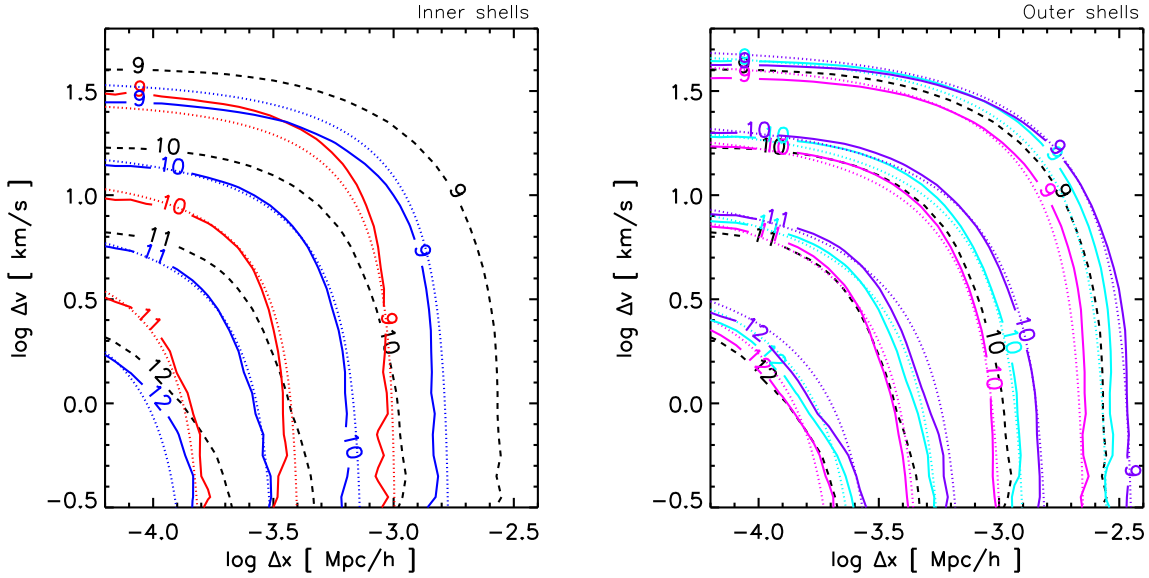


**Figure 9.** Contours of the logarithm of the particle phase space average density ( $P^2SAD$ ) for the Aq-A-2 halo at  $z = 0$  for samples of particles taken at different radial shells from the halo centre. *Left panel:*  $0 < r/r_{200} < 0.2$  (red) and  $0.2 < r/r_{200} < 0.4$  (blue). *Right panel:*  $0.4 < r/r_{200} < 0.6$  (magenta),  $0.6 < r/r_{200} < 0.8$  (cyan), and  $0.8 < r/r_{200} < 1.0$  (violet). A sample of eight million particles was used for each shell. The dotted lines are fits given by Eqs. 11-12 with the parameters shown in table 3. For reference, the dashed line is  $P^2SAD$  averaged over the whole halo (i.e., the black solid line in Fig. 4).

show the contours of  $\log(P^2SAD)$  for  $z = 0$  (left) and  $z = 3.5$  (right). There are important differences relative to the case we explored before:

- Looking at Fig. 7, we see that at large  $\Delta v$  there is almost no redshift evolution possibly because  $P^2SAD$  is dominated by particles outside the main halo that undergo little merging and/or tidal disruption. We should note that by

taking the average of  $P^2SAD$  over all velocity separations  $\Delta v$ , one is probing the spatial 2PCF. By doing so we also find a (near) lack of evolution, which might be taken as evidence for the original (position-space) stable clustering hypothesis (Davis & Peebles 1977).

- There is a clear “bump”, more prominent at higher redshifts, where the contours of constant phase space density bend, related to the Hubble flow, which, at fixed physical



$r/r_{200}$	$\beta$	$q_X(\text{Mpc}/h)$	$\alpha_X$	$q_V(\text{km}/s)$	$\alpha_V$
0.0-0.2	1.0	4.06	-0.40	$4.0 \times 10^4$	-0.35
0.2-0.4	0.9	2.97	-0.36	$3.34 \times 10^4$	-0.33
0.4-0.6	0.8	2.63	-0.34	$4.1 \times 10^4$	-0.33
0.6-0.8	0.775	3.29	-0.34	$5.6 \times 10^4$	-0.34
0.8-1.0	0.75	5.14	-0.35	$5.9 \times 10^4$	-0.34

**Table 3.** Values of the parameters in Eq. 12 for the fit to  $P^2SAD$  averaged over different radial shells centered in the Aq-A-2 halo as indicated in the first column (see Fig.9).

separation, is more important at high redshifts. The latter is clearly demonstrated by the straight orange line in Fig. 7 that shows the Hubble flow for  $z = 3.5$ .

- Interestingly, at small  $\Delta v$ , a less dense environment, increases the average value of  $P^2SAD$ , presumably because the low-mass field haloes (which are substantially denser in phase space) contribute most to the average. That is, the 1-(sub)halo term in  $P^2SAD$  receives additional contributions from low-mass field haloes and their subhaloes, and also the 2-halo term appears as a novel contribution, particularly for large  $\Delta x$ . This is a likely explanation for most of the difference between the dashed and solid lines in Fig. 8, and also explains why only the velocity axis evolves for the halo region, while both axes evolve for the larger region. Notice how for the smallest values of  $\Delta x$ , the volume average seems to converge in both cases.

Let us now consider denser environments for the average of  $P^2SAD$  by taking concentric shells of increasing volume within the halo. In particular, we take five radial shells with the same thickness:  $0.2 r_{200}$ , and consider only the case at  $z = 0$ . The left (right) panel of Fig 9 shows the contours of  $\log(P^2SAD)$  for the first (last) two (three) shells. For reference we show in both panels the result of the average within the virialized region of the halo with a black dashed line (corresponding to the black solid line of Fig. 4). Overall, there is a trend of increasing phase space density towards the periphery of the halo. This is clearly connected to the increasing total number of subhaloes as a function of radius, since it is well known that the mean/characteristic phase space density of the main (or spherically averaged) halo decreases in the outer parts (e.g. Taylor & Navarro 2001). Closer to the halo centre, tidal stripping has been more effective in destroying subhaloes diluting the average value of  $P^2SAD$ . Subhalo abundance and the radial-dependent tidal stripping also explain the clear change in the shape of the iso- $P^2SAD$  contours, with the ones corresponding to the outer shells being rounder due to the increasing number of subhaloes, while the inner shells have a shape closer to the smooth halo component (see contour plot in Fig. 3). Notice that within the third shell (i.e.  $0.4 < r/r_{200} < 0.6$ ),  $P^2SAD$  is very close to the average within the whole halo.

The changes in shape and normalization of  $P^2SAD$  for the different radial shells can be captured accurately by the fitting functions provided in Eqs. (11-12) with the parameters given in Table 3.

### 3.5 Formation history: different Aquarius haloes

Fig. 10 shows the variation of the particle phase space average density in the different Aquarius haloes at resolution level 4 at different redshifts according to the legends in the top right corner of each panel. These are MW-like haloes with different masses at  $z = 0$ :  $M_{200} \in (0.8, 1.8)10^{12} M_{\odot}$  (see Table 1), concentrations that vary up to a factor of two, and very different mass aggregation histories representing a wide range of the full distribution expected for haloes of this mass in a cosmological volume (see Figs. 2 and 3 of Boylan-Kolchin et al. 2010, for ease of comparison we have used their color scheme in Fig. 10). The upper panel is for the volume average within the halo while the lower panel is for a larger volume given by the Lagrangian region of the high-resolution particles at  $z = 0$ . It is remarkable that despite the diverse merger histories,  $P^2SAD$  seems to be universal, particularly at small separations where the contours of constant  $\log(P^2SAD)$  of the different haloes are very close to each other with small variations in redshift up to  $z \sim 2$ . It is important to remark that at level 4 of resolution,  $P^2SAD$  is only converged for  $\log(P^2SAD) \sim 9$  (see Fig. A1), and thus the results at higher values of  $P^2SAD$ , although suggestive, should be taken with care. Nevertheless, this resolution is enough to probe the regime where subhaloes start to dominate and point towards the universality we mentioned before.

Although we do not explore this further, at large  $\Delta v$ , the difference in the contours of phase space density at a given redshift is due to the different properties of the smooth distribution, while variations across different redshifts seem to be correlated with the mass aggregation history of the halo. The fact that the difference between different haloes is smaller for the larger volume (lower panels of Fig. 10) seems to support the latter.

## 4 SUMMARY AND CONCLUSIONS

We provide a different perspective on the clustering of dark matter in phase space by introducing the Particle Phase Space Average Density:  $P^2SAD \equiv \Xi(\Delta x, \Delta v)$ . This quantity is defined as the 2D two-point correlation function (2PCF) in phase space divided by the mean phase space density within the phase space volume where the average is made (see Eqs. 1-2). It is thus a generalization of the concept of the 2PCF in position space as a measure of the number of particle pairs separated by a distance  $\Delta x$  in space and  $\Delta v$  in velocity space.

We analyse the structure of  $P^2SAD$  in galactic haloes by using the simulation suite of the Aquarius project (Springel et al. 2008) and find the following main results:

- The structure of  $P^2SAD$  averaged within the virialized halo is divided into two distinct regions corresponding to the smooth dark matter distribution at large separations in phase space and to “all” the hierarchy of substructures at small separations (see Fig. 3).
- Most of the evolution of  $P^2SAD$  across time occurs at large separations and is roughly understood by the “inside-out” growth of the smooth dark matter halo.
- In the regime where gravitationally bound substructures

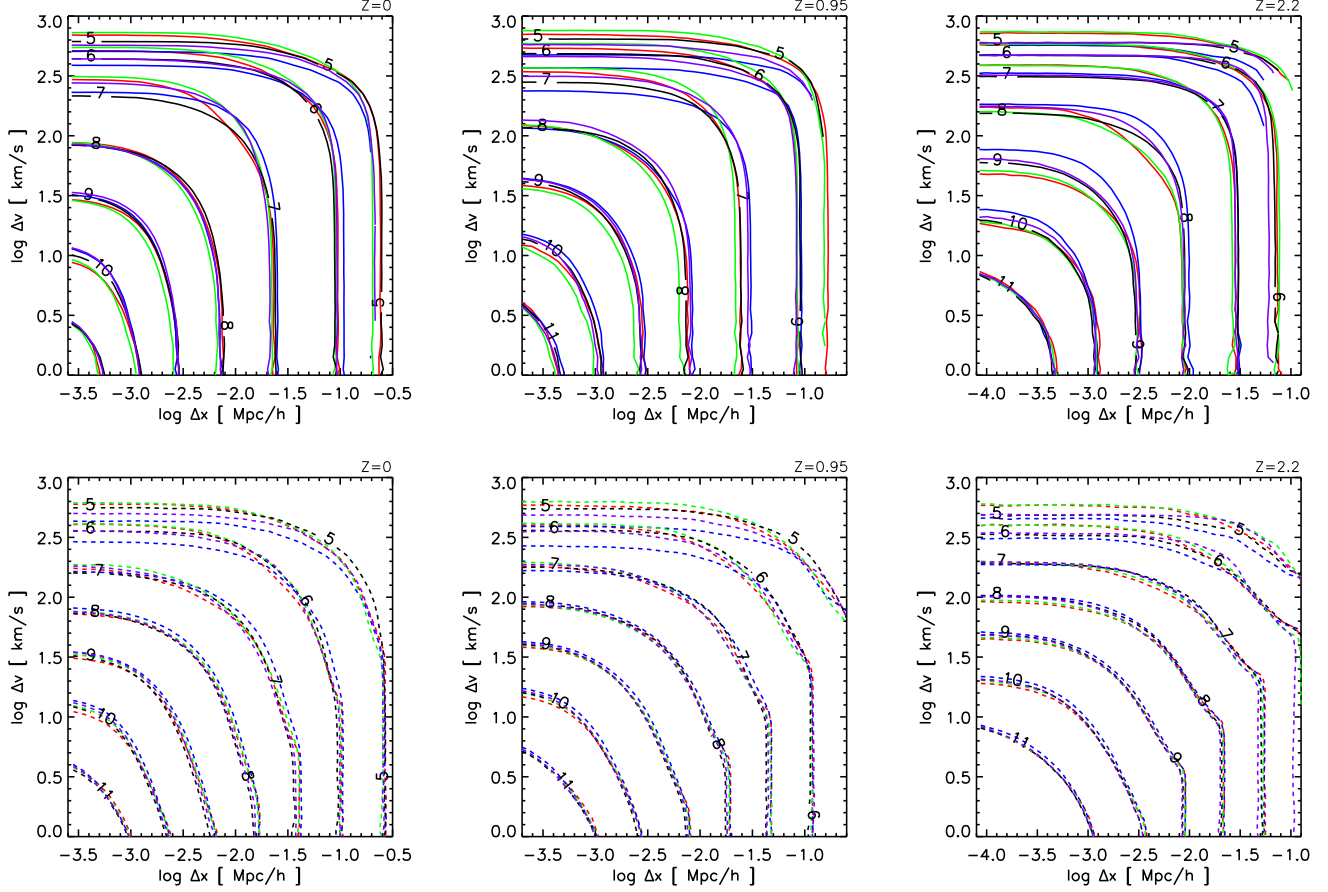


**Figure 10.** Contours of the particle phase space average density ( $P^2SAD$ ) for the Aquarius haloes: Aq-A (red), Aq-B (blue), Aq-C (green), Aq-D (black), Aq-E (violet) at different redshifts:  $z = 0$  (left),  $z = 0.96$  (middle) and  $z = 2.2$  (right). In the upper panels, only particles within the main halo and its subhaloes are considered at each redshift while in the bottom panels, all the high-resolution particles at  $z = 0$  are considered for all redshifts (see Fig.7 and Section 3.4). In all cases the resolution level is 4. Note the change in the range of the horizontal axis in the different panels.

tures dominate, there is a remarkable nearly universal behaviour of  $P^2SAD$  across:

- *Time* (Fig. 4), with variations of a factor  $\lesssim 3$  between  $z = 0$  and  $z = 3.5$ , while the average density within the halo changes by a factor of  $\sim 30$ .
- *Ambient density* (Figs. 8-9), varying by a factor of  $\sim 30$  at the most, while the average density changes by nearly four orders of magnitude.
- *Mass accretion histories* (Fig. 10). The structure of  $P^2SAD$  changes only slightly for the five MW-size haloes we analyzed (typically much less than a factor of 2), despite of their diverse mass accretion histories, and subhalo distributions.

- In the small scale regime we found that  $P^2SAD$  can be described by a family of superellipse contours in the  $(\Delta x, \Delta v)$  plane with axes that scale with the phase space density as power laws (see Eqs. 11-12). By introducing slow variations in redshift and halo-centric distance for the parameters in the superellipse, we are able to obtain good fits to the simulation data in all cases.

The functional shape that fits the structure of  $P^2SAD$  at small separations is inspired by a model based

on an extension into phase space of the stable clustering hypothesis, originally introduced by Davis & Peebles (1977) in position space. In a companion paper (Zavala & Afshordi 2013), we describe this model in great detail and show how, coupled with a simplified tidal disruption scenario, it can describe the simulation data quite well.

Although we have shown that  $P^2SAD$  is sensitive to cold small scale gravitationally bound subhaloes, we want to remark that  $P^2SAD$  is not a substitute for a substructure finder, but rather an alternative way of studying dark matter clustering. This is similar to contrasting a measurement of the galaxy two-point correlation function, with identifying groups and clusters of galaxies, and their statistics. As is well known in the studies of large scale structure, the two contain complementary (but to some extent overlapping) information.

The structure of  $P^2SAD$  is useful to obtain predictions for non-gravitational signatures of dark matter. In particular, the annihilation rate can be written as an integral over all relative velocities in the limit of relative distance going to zero. In paper II of this series (Zavala & Afshordi 2013) we show how this can be used to obtain predictions for annihilation signals for general velocity-dependent cross-sections.

## ACKNOWLEDGMENTS

We are grateful to the anonymous reviewer for useful suggestions and comments. We thank the members of the Virgo consortium for access to the Aquarius simulation suite and our special thanks to Volker Springel for providing access to SUBFIND and GADGET-3 whose routines on the computation of the 2PCF in real space were used as a basis for the code in phase space we developed. We also thank Simon White, Ed Bertschinger and Steen Hansen for useful suggestions. JZ and NA are supported by the University of Waterloo and the Perimeter Institute for Theoretical Physics. Research at Perimeter Institute is supported by the Government of Canada through Industry Canada and by the Province of Ontario through the Ministry of Research and Innovation. JZ acknowledges financial support by a CITA National Fellowship. This work was made possible by the facilities of the Shared Hierarchical Academic Research Computing Network (SHARCNET:www.sharcnet.ca) and Compute/Calcul Canada.

## REFERENCES

- Afshordi N., Mohayaee R., Bertschinger E., 2009, *Phys. Rev. D*, 79, 083526
- Afshordi N., Mohayaee R., Bertschinger E., 2010, *Phys. Rev. D*, 81, 101301
- Arkani-Hamed N., Finkbeiner D. P., Slatyer T. R., Weiner N., 2009, *Phys. Rev. D*, 79, 015014
- Bertschinger E., 1985, *ApJS*, 58, 39
- Boylan-Kolchin M., Springel V., White S. D. M., Jenkins A., 2010, *MNRAS*, 406, 896
- Boylan-Kolchin M., Springel V., White S. D. M., Jenkins A., Lemson G., 2009, *MNRAS*, 398, 1150
- Davis M., Peebles P. J. E., 1977, *ApJS*, 34, 425
- Diemand J., Kuhlen M., 2008, *ApJ*, 680, L25
- Gao L., Frenk C. S., Boylan-Kolchin M., Jenkins A., Springel V., White S. D. M., 2011, *MNRAS*, 410, 2309
- Maciejewski M., Vogelsberger M., White S. D. M., Springel V., 2011, *MNRAS*, 415, 2475
- Navarro J. F., Frenk C. S., White S. D. M., 1996, *ApJ*, 462, 563
- Navarro J. F., Frenk C. S., White S. D. M., 1997, *ApJ*, 490, 493
- Navarro J. F., Ludlow A., Springel V., Wang J., Vogelsberger M., White S. D. M., Jenkins A., Frenk C. S., Helmi A., 2010, *MNRAS*, 402, 21
- Springel V., Wang J., Vogelsberger M., Ludlow A., Jenkins A., Helmi A., Navarro J. F., Frenk C. S., White S. D. M., 2008, *MNRAS*, 391, 1685
- Springel V., White S. D. M., Tormen G., Kauffmann G., 2001, *MNRAS*, 328, 726
- Taylor J. E., Navarro J. F., 2001, *ApJ*, 563, 483
- Vera-Ciro C. A., Helmi A., Starkenburg E., Breddels M. A., 2013, *MNRAS*, 428, 1696
- Vogelsberger M., Helmi A., Springel V., White S. D. M., Wang J., Frenk C. S., Jenkins A., Ludlow A., Navarro J. F., 2009, *MNRAS*, 395, 797
- Vogelsberger M., White S. D. M., 2011, *MNRAS*, 413, 1419
- Vogelsberger M., White S. D. M., Helmi A., Springel V., 2008, *MNRAS*, 385, 236

Zavala J., Afshordi N., 2013, arXiv:1311.3296

## APPENDIX A: CONVERGENCE TESTS

Fig. A1 shows the particle phase space average density ( $P^2SAD$ ) computed with our algorithm for the Aq-A halo at different resolutions, from level 5 (dashed-dotted line) to level 2 (solid line). The upper-left ( $z = 0$ ), lower-left ( $z = 0.95$ ) and bottom-right ( $z = 2.2$ ) panels show the case where particles in the main halo and its subhaloes contribute to the average, while the upper-right panel ( $z = 0$ ) considers only particles within the main halo. As we mentioned in Section 3.1, the main host dominates  $P^2SAD$  at large  $(\Delta x, \Delta v)$ , while at smaller scales, the contribution of the smooth halo is subdominant and it is of course resolution dependent, since simulation particles that are part of the smooth component at low resolutions can form bound subhaloes at higher resolutions. This is clearly shown in the right panel of Fig. A1. At large  $(\Delta x, \Delta v)$ , the value has clearly converged, but at small separations in phase space, the smooth component is ever decreasing with increasing resolution. On the contrary,  $P^2SAD$  for both the smooth and subhalo components (upper-left panel) is roughly convergent until the value of the separation that can be resolved for a given resolution. By increasing the resolution, the values that  $P^2SAD$  can take are larger and larger reaching smaller and smaller separations in phase space. We also note that sampling errors (a random number of particles  $N_s$  is used to estimate  $P^2SAD$ , see Section 2.1) are negligible. This can be seen by noticing that although we keep the samples of particles fixed to a few millions for the simulations across different resolutions, these samples are of course chosen at random in *each* simulation. If sampling errors were an issue, then convergence at large separations in phase space would be much poorer. We have nevertheless tested this explicitly taking larger samples and found no significant difference in our results.

The spatial resolution of each simulation is roughly characterized by the scale at which the gravitation law is “softened”  $\sim 2.8\epsilon$ , where  $\epsilon$  is the Plummer-equivalent gravitational softening length. Since we are dealing with convergence in phase space we determine instead the region in phase space where  $P^2SAD$  has converged by over-plotting in Fig. A1 contours of constant ratio of  $P^2SAD$  between consecutive resolution levels, e.g. a ratio of 1.25 between resolution levels 3 and 2 is given by a magenta dotted line. We only do so for two values of this ratio, 1.25 and 1.5. By looking at the contours for a fixed value of this ratio at increasing resolution we can confidently establish that for level 2, resolution is not an issue for most of the region in phase space explored in this paper.

Fig. A2 shows the convergence for  $P^2SAD$  averaged over different volumes corresponding to concentric shells of thickness  $0.2r_{200}$  from the centre of the halo. All particles within a given shell are considered for two resolution levels at  $z = 0$ : level 3 (dashed) and level 2 (solid). Although the results seem to converge across resolutions, they do so with larger deviations compared to when the average is taken within larger volumes. This is likely related to the fluctuations in subhalo abundance as a function of radius (see e.g. the middle panel of Fig. 12 of Springel et al. 2008).

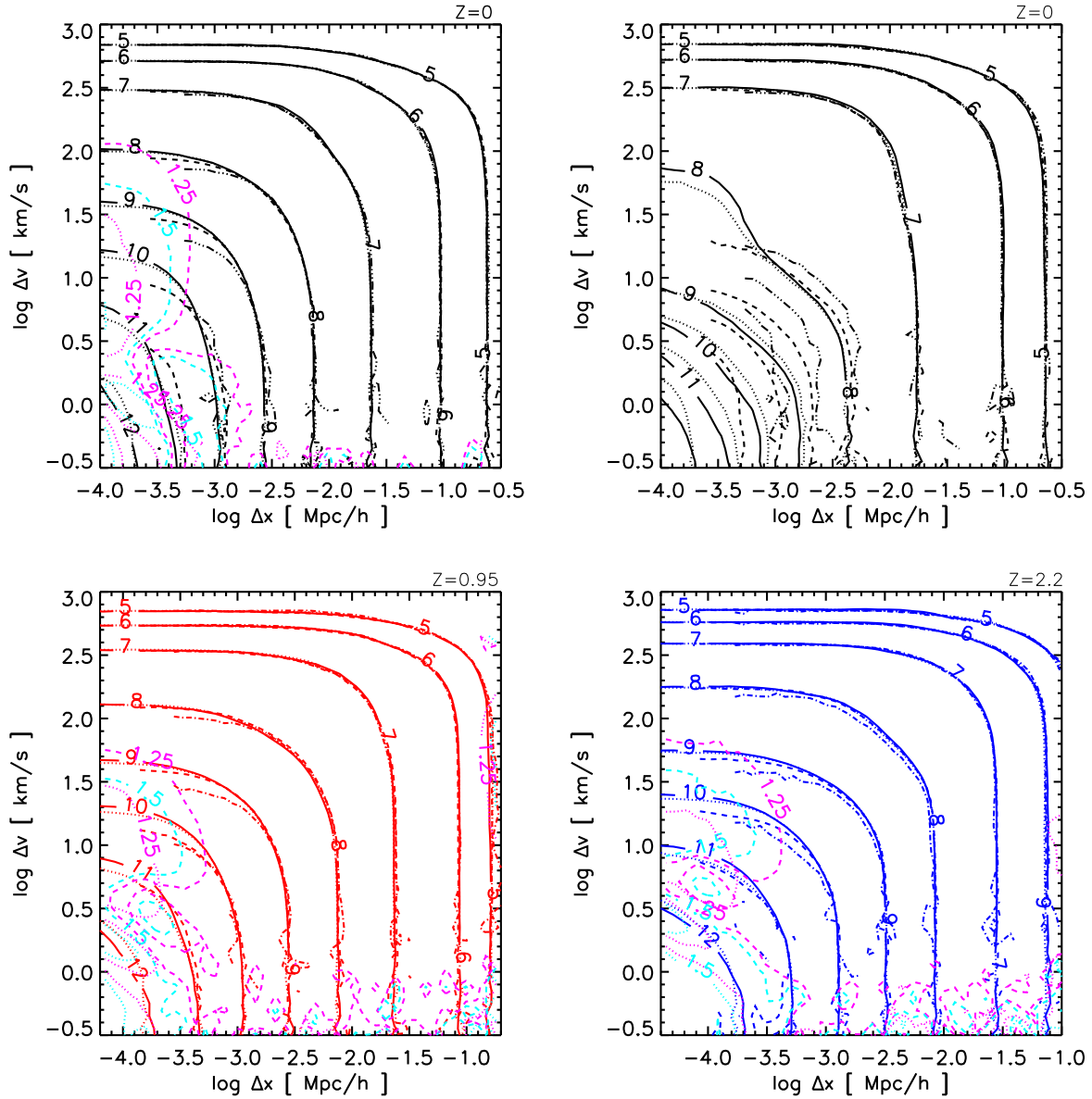


**Figure A1.** Contours of the logarithm of the particle phase space average density ( $P^2SAD$ ) for the Aquarius A-halo at different resolutions levels: 2 (solid), 3 (dotted), 4 (dashed) and 5 (dotted-dashed). *Upper panels:* At  $z = 0$  for the main halo and its subhaloes (left) and for the main halo only (right). *Bottom panels:*  $z = 0.95$  (red, left),  $z = 2.2$  (blue, right) for the main halo and its subhaloes. The magenta and cyan contours mark the regions where the value of the coarse-grained phase space density between two consecutive resolution levels (excluding level 5 since it is dominated by noise at small separations in velocity) is a factor of 1.25 and 1.5, respectively: 3 and 4 (dashed), 2 and 3 (dotted).

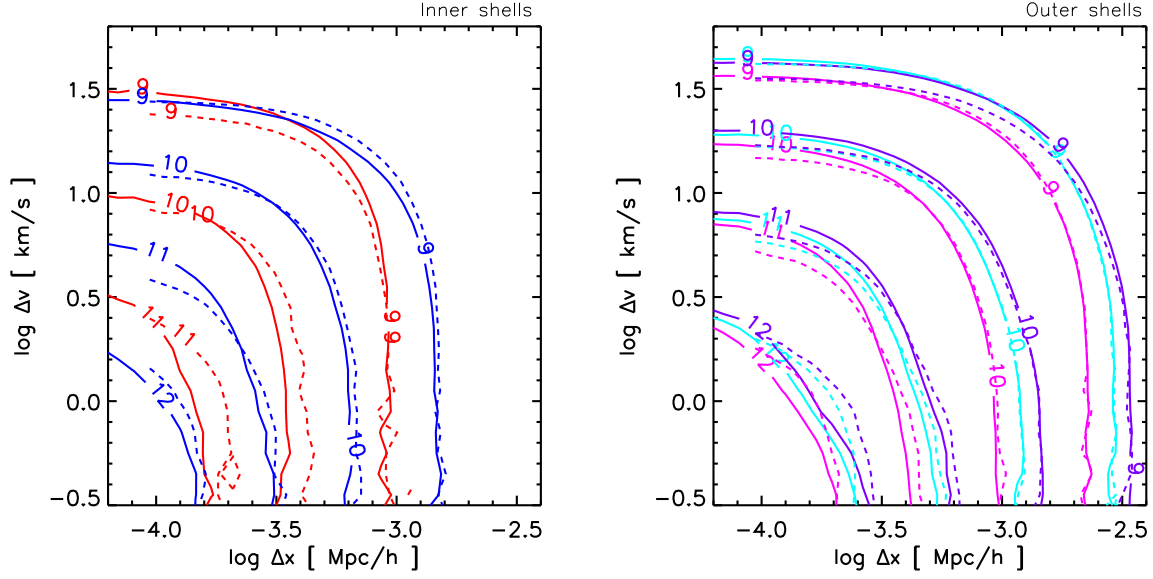


**Figure A2.** Contours of the logarithm of the particle phase space average density ( $P^2SAD$ ) for the Aquarius A-halo at  $z = 0$  for two different resolution levels: Aq-A-3 (dashed) and Aq-A-2 (solid), at different radial shells from the halo centre:  $0 < r/r_{200} < 0.2$  (red, left),  $0.2 < r/r_{200} < 0.4$  (blue, left),  $0.4 < r/r_{200} < 0.6$  (magenta, right),  $0.6 < r/r_{200} < 0.8$  (cyan, right), and  $0.8 < r/r_{200} < 1.0$  (violet, right).